






Semi-analytical model for electrically injected GaAs nano-ridge laser diodes monolithically integrated on silicon

ANDUALEM ALI YIMAM,^{1,*} DAVIDE COLUCCI,^{1,2}  CHARLES CAER,^{2,3}  DIDIT YUDISTIRA,² YANNICK DE KONINCK,^{2,4} HUSEYIN SAR,² MARINA BARYSHNIKOVA,² PETER VERHEYEN,² JORIS VAN CAMPENHOUT,² BERNARDETTE KUNERT,² GEERT MORTHIER,¹ AND DRIES VAN THOURHOUT¹ 

¹Department of Information Technology (INTEC), Photonics Research Group, Ghent University-imec, Technologiepark-Zwijnaarde 126, 9052 Ghent, Belgium

²imec, Kapeldreef 75, 3001 Heverlee, Leuven, Belgium

³Present address: Centre Suisse d'Electronique et de Microtechnique SA (CSEM), CH-2002 Neuchâtel, Switzerland

⁴Present address: NVidia Corporation, Roskilde 4000, Denmark

*ayimam.yimam@ugent.be

Abstract: We present a semi-analytical model that can accurately explain the working principle behind the recently reported electrically injected In_{0.2}Ga_{0.8}As/GaAs monolithic nano-ridge lasers and more importantly show how the model can be used to study the effect of device parameters on the spectral behavior, the slope efficiency and the threshold gain. We show that mode beating between the fundamental mode and a higher order mode is fundamental in the operation of these lasers. Analytical expressions for codirectional mode coupling are used in developing the round-trip laser model. Results from analytical expressions are verified by comparisons with simulations and the model is supported later by measurement results.

© 2025 Optica Publishing Group under the terms of the [Optica Open Access Publishing Agreement](#)

1. Introduction

Since its inception [1], the field of silicon photonics has garnered significant attention [2–4] and continues to expand rapidly, driven by its vast potential to leverage the matured silicon complementary metal-oxide semiconductor (CMOS) processing technology and its capability in addressing the ever-increasing demand for large bandwidth. These features have opened avenues for high production yield and substantial reduction in cost, particularly in optical interconnects applications [5–7].

But there is one major Achilles heel in the field of silicon photonics: silicon is an indirect bandgap semiconductor; hence a poor light emitter. This has led to the exploration of different mechanisms to integrate high gain direct bandgap III-V materials on silicon including hybrid flip-chip bonding [8], heterogenous die-to-wafer bonding [9–11] and transfer printing [12–14]. Compared to these approaches, the monolithic integration of III-V materials on silicon is deemed the ultimate integration technique with regard to cost effective integration and scalability. However, the large mismatch in crystal lattice constants, thermal expansion coefficients and polarity between silicon and most III-V compounds leads to misfit defects, threading dislocations and planar defects, severely affecting the carrier lifetime, and thereby hampering efficient light emission [15]. To mitigate these issues, extensive work has been conducted over the last two decades utilizing buffer layers to confine defects and prevent them from reaching the active region [16–19] and using different versions of selective area growth [20–23].

By employing selective area growth over confined regions to restrict defects in narrow oxide trenches, followed by the outgrowth of III-V material for high modal gain using nano-ridge engineering [24], optically pumped $\text{In}_{0.2}\text{Ga}_{0.8}\text{As}/\text{GaAs}$ multi-quantum well nano-ridge lasers emitting around 1020 nm have been demonstrated [25]. By increasing the In content in the quantum wells ($\text{In}_{0.45}\text{Ga}_{0.55}\text{As}$) in an $\text{In}_{0.25}\text{Ga}_{0.75}\text{As}$ nano-ridge base, the lasing emission was extended to the O-band (1300 nm) [26]. Given the small dimensions of these devices, electrical pumping has so far proved very difficult but was recently demonstrated exploiting a mode beating effect to reduce losses [27]. Continuous-wave lasing at room temperature was demonstrated for these nano-ridge laser arrays with emission wavelength around 1020 nm. In these lasers, three $\text{In}_{0.2}\text{Ga}_{0.8}\text{As}$ quantum wells (QW's) were used as gain material in a GaAs base and an InGaP passivation layer was used to effectively suppress surface recombination. GaAs p-i-n diodes were realized by a heavily doped n-type Si surface on which the n-type GaAs trench region is grown as well as a p-type GaAs top layer. The p-type contact is formed by an array of tungsten plugs that pierce the InGaP cap and land on the p-type GaAs while the n-type contact is formed by a tungsten contact that lands on the n-type Si. The pitch of the p-type contact grating is carefully designed to create a loss dip that enables laser operation. The loss dip originates from beating between the fundamental mode and a higher order mode.

Here, we present a semi-analytical model for these electrically injected $\text{In}_{0.2}\text{Ga}_{0.8}\text{As}/\text{GaAs}$ nano-ridge lasers. The model helps not only in understanding the internal operation of these devices but also in optimizing the cross-section of the device and the contacting scheme to obtain low threshold gain and a predefined emission wavelength. We find that beating between two modes of the nano-ridge is central in the lasing operation. This mode beating is very sensitive to small effective index changes. In that respect, more accurate laser parameters and optimized device dimensions can be obtained by the model. In the organization of this paper, we will employ a step by step approach starting with the derivation of analytical expressions for mode coupling in a nano-ridge waveguide in the second section, developing a round-trip laser model in section 3 and verifying the model with experimental results in section 4. We close with a conclusion in section 5.

2. Coupling between modes in a nano-ridge waveguide

We consider a nano-ridge waveguide with a periodic array of tungsten plugs (with a contact pitch of $4.8 \mu\text{m}$ and permittivity of $-4.31 + i21.89$ around 1035 nm) for current injection, integrated on top as shown in Figure 1(a), and having a cross-section as shown in Figure 1(b), with relevant parameters defined in Table 1. The indicated doping profile is not taken into account at this stage and will be used in section 3. Computing eigenmodes with Lumerical MODE solver [28] at a wavelength of $1.035 \mu\text{m}$ yields multiple higher order modes with different effective indices, as depicted in Figure 1(c). The first mode, which is the fundamental quasi-TM (transverse magnetic) mode, is more extended in the vertical direction and hence has larger leakage loss to the silicon substrate. The second mode is the fundamental quasi-TE (transverse electric) mode, which will be discussed further in this paper due to its lower leakage loss and highest confinement factor. This has also been verified in [25]. The others are higher order TEM modes, where "TEM" represents hybrid modes that are partially TE and partially TM.

Table 1. Parameters for GaAs nano-ridge cross-section in Fig. 1(b)

a (nm)	b (nm)	c (nm)	d (nm)	e (nm)	f (nm)	g (nm)	h (nm)
490	400	265	125	100	100	222	308

Using the FDTD solver, we evaluated the power decay for the TE₀₀ mode travelling through this structure by putting a modal source at $z = 0$ and power monitors at $z = 50 \mu\text{m}$ and $z = 100 \mu\text{m}$. Figure 1(d) shows the spectrum for the power attenuation calculated by recording the power

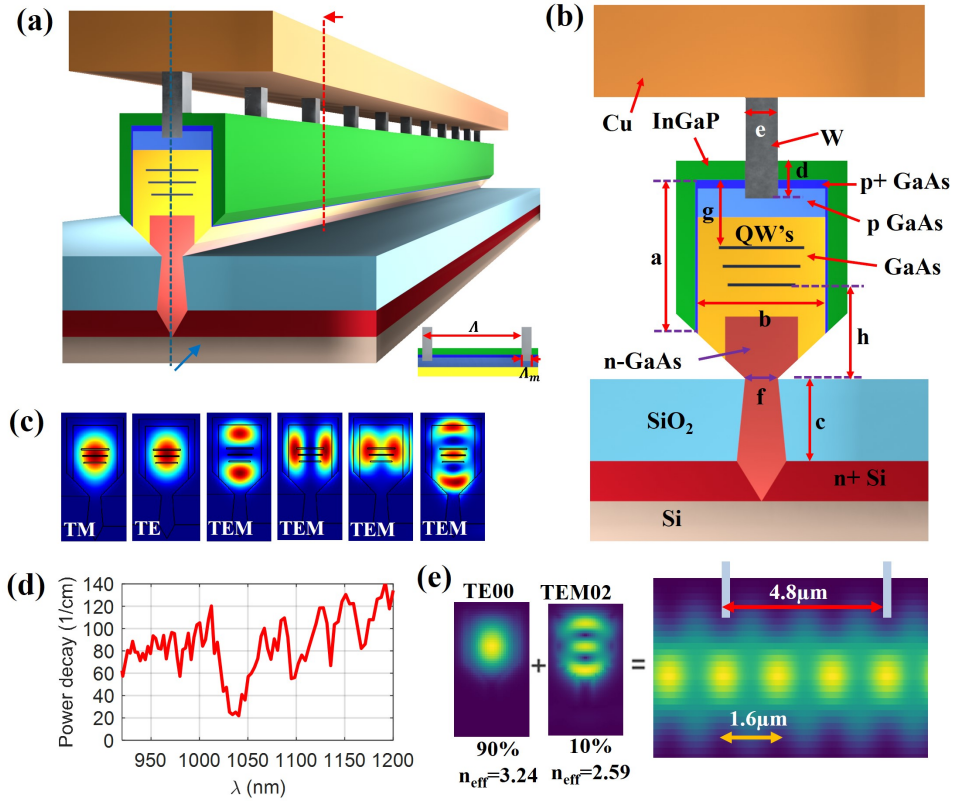


Fig. 1. (a) Schematic of a nano-ridge waveguide with a tungsten metal grating, $\Lambda=4.8 \mu\text{m}$ and $\Lambda_m=100 \text{ nm}$ (not to scale). (b) Cross-sectional schematic of the nano-ridge waveguide at a position of a tungsten metal plug (indicated by the red dotted line in (a)) with dimensions shown in Table 1 and doping levels of $2 \times 10^{18} \text{ cm}^{-3}$ for p-GaAs, $1 \times 10^{19} \text{ cm}^{-3}$ for p+ GaAs, $2 \times 10^{18} \text{ cm}^{-3}$ for n-GaAs and $1 \times 10^{19} \text{ cm}^{-3}$ for n+ Si. (c) Modes supported in a nano-ridge transversal cross-section calculated by Lumerical FDE solver at a position where there is no metal plug. (d) Calculated power decay of the TE00 mode from power monitors placed at $z = 50 \mu\text{m}$ and $z = 100 \mu\text{m}$. (e) Mode beating pattern from the interference of the TE00 and TEM02 modes with a beating length of $1.6 \mu\text{m}$ at $1.035 \mu\text{m}$ wavelength showing low intensity zones just below metal contacts.

decay of the TE00 mode between the monitors at $z = 50 \mu\text{m}$ and $z = 100 \mu\text{m}$. We can clearly see dips in the transmission spectrum. Inspecting the longitudinal field pattern at $1.035 \mu\text{m}$, the wavelength with the lowest attenuation, we notice an interference pattern with a beating length of $1.6 \mu\text{m}$ as shown in Figure 1(e). Further inspection reveals that this pattern originates from beating between the TE00 and TEM02 modes and results in a reduced overlap with the lossy metal.

Now, having this background information from the numerical simulations, this section will be devoted to the derivation of appropriate analytical expressions explaining these phenomena. These results will be crucial in developing the round-trip laser model in the next section.

Considering two dominant modes in the nano-ridge waveguide, the total electric field in the waveguide is given by

$$E(x, y, z) = E_1(z)U_1(x, y)e^{-j\beta_1 z} + E_2(z)U_2(x, y)e^{-j\beta_2 z} \quad (1)$$

where $U_1(x, y)$ and $U_2(x, y)$ are the transversal mode profiles of the two dominant modes of the unperturbed waveguide, β_1 and β_2 are the unperturbed propagation constants of the modes and E_1 and E_2 are the mode amplitudes.

Using the Helmholtz equation for the total electric field and assuming a periodic perturbation $\Delta \epsilon$ of the relative permittivity, we can derive the following coupled wave equations [29].

$$\frac{dE_1(z)}{dz} = -j \frac{\kappa_0^2}{2\beta_1} E_1 \frac{\int \Delta \epsilon U_1^2 dA}{\int U_1^2 dA} - j \frac{\kappa_0^2}{2\beta_1} e^{-j(\beta_2 - \beta_1)z} E_2 \frac{\int \Delta \epsilon U_1 U_2 dA}{\int U_1^2 dA} \quad (2)$$

$$\frac{dE_2(z)}{dz} = -j \frac{\kappa_0^2}{2\beta_2} E_2 \frac{\int \Delta \epsilon U_2^2 dA}{\int U_2^2 dA} - j \frac{\kappa_0^2}{2\beta_2} e^{-j(\beta_1 - \beta_2)z} E_1 \frac{\int \Delta \epsilon U_1 U_2 dA}{\int U_2^2 dA} \quad (3)$$

where κ_0 is the free-space propagation constant.

Now, we can expand the periodic perturbation, $\Delta \epsilon$, in a Fourier series of the form

$$\Delta \epsilon(x, y, z) = \sum_{l=-\infty}^{l=+\infty} \Delta \epsilon_l(x, y) e^{-jl(\frac{2\pi}{\Lambda})z} \quad (4)$$

where $l(\frac{2\pi}{\Lambda})$ are the spatial harmonics of the perturbation with a fundamental period Λ (as shown in Figure 1(a)) and l is an integer.

We can then readily express (2) and (3), by keeping only the slowly varying terms, as

$$\frac{dE_1(z)}{dz} = -j\kappa_{11}E_1 - j\kappa_{12}E_2 e^{j(\beta_1 - \beta_2 - l\frac{2\pi}{\Lambda})z} \quad (5)$$

$$\frac{dE_2(z)}{dz} = -j\kappa_{22}E_2 - j\kappa_{21}E_1 e^{j(\beta_2 - \beta_1 + l\frac{2\pi}{\Lambda})z} \quad (6)$$

where $\kappa_{ii} = \frac{\kappa_0^2 \int \Delta \epsilon_i U_i^2 dA}{2\beta_i \int U_i^2 dA}$, $\kappa_{12} = \frac{\kappa_0^2 \int \Delta \epsilon_{-l} U_1 U_2 dA}{2\beta_1 \int U_1^2 dA}$, $\kappa_{21} = \frac{\kappa_0^2 \int \Delta \epsilon_l U_1 U_2 dA}{2\beta_2 \int U_2^2 dA}$, $i = 1, 2$, and l is the integer for which $\beta_1 - \beta_2 \approx l\frac{2\pi}{\Lambda}$.

As $\Delta \epsilon_l = \Delta \epsilon_{-l}$ for a perturbation with symmetry around $z = 0$, $\kappa_{12} = \kappa_{21}$ provided that we have normalization of modes with respect to power according to $\beta_i \iint U_i^2 dx dy = 2\mu_0\omega$, where $i = 1, 2$, μ_0 is the permeability of free space and ω is angular frequency.

κ_{11} and κ_{22} are the self-coupling terms originating from the difference in the effective indices between the modes of the perturbed and the unperturbed waveguide. κ_{12} and κ_{21} determine the coupling between the modes.

As the interference between the TE00 and the TEM02 modes is the root cause of the beating pattern shown in Figure 1(e), we analyzed the power coupling from the TE00 mode to the TEM02 mode when we launch the TE00 mode at $z = 0$. In that case, the normalized power of the modes at a position z from the source can be calculated by solving the coupled differential equations, (5) and (6), for the electric field of the modes. The powers in the TE00 and the TEM02 modes respectively become

$$P_1(z) = \left| \cos(sz) - j \frac{\delta}{s} \sin(sz) \right|^2 e^{-2Im(\tilde{\beta})z} \quad (7)$$

$$P_2(z) = \left| \frac{\kappa_{21}}{s} \sin(sz) \right|^2 e^{-2Im(\tilde{\beta})z} \quad (8)$$

where $\tilde{\beta} = \frac{\beta_1 + \kappa_{11} + \beta_2 + \kappa_{22}}{2}$, $\delta = \frac{\beta_1 + \kappa_{11} - \beta_2 - \kappa_{22}}{2} - l\frac{\pi}{\Lambda}$, $s = \sqrt{\delta^2 + \kappa_{12}\kappa_{21}}$, $\beta_1 = \frac{2\pi n_1}{\lambda}$ and $\beta_2 = \frac{2\pi n_2}{\lambda}$.

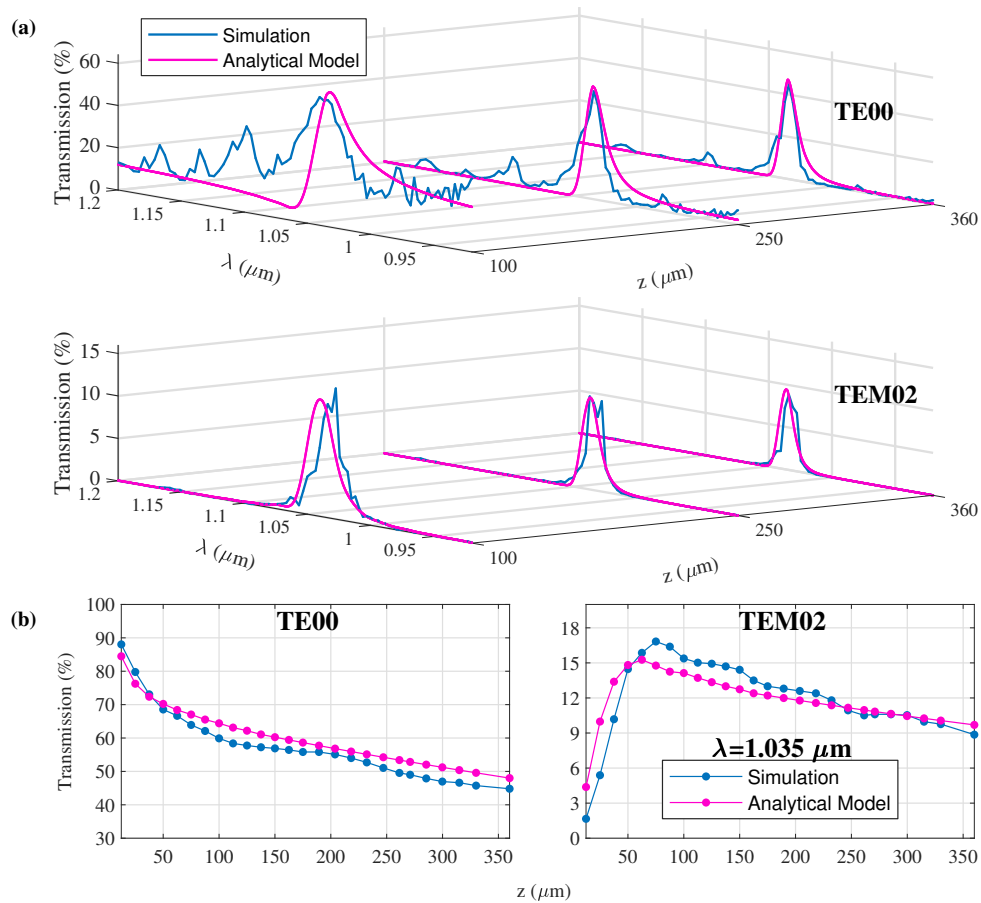


Fig. 2. Comparison between analytical results and simulation results of: (a) TE00 and TEM02 mode power spectra at different positions along the length of the nano-ridge waveguide. (b) TE00 and TEM02 mode power at zero detuning wavelength at different z positions from the source.

Note that all the terms $\tilde{\beta}$, δ , s , β_1 , β_2 and the coupling coefficients are wavelength dependent. n_1 and n_2 are the unperturbed effective indices of the two modes in the nano-ridge.

Exporting electric field data, effective refractive indices for the two modes and permittivity data from a mode solver (Lumerical Mode) and calculating overlap integrals by performing numerical integration in Matlab (considering a complex perturbation with a rectangular $\Delta\epsilon$ profile as in Fig. 1 (a)), we evaluated the coupling coefficients and calculated the power spectrum of the two modes at different positions from the source and compared these results with FDTD simulation results.

Figure 2(a) shows a comparison between the analytical results and the simulation results for the power in the TE00 and TEM02 modes in the 920–1200 nm wavelength range at different positions along the length of the nano-ridge. Figure 2(b) shows the comparison for the maximum power of the modes (at the wavelength of zero detuning) at different positions along the nano-ridge length. We can observe from these graphs that around the $1.035 \mu\text{m}$ wavelength, where the coupling between the TE00 and the TEM02 modes occurs, the results from the analytical expressions and the simulations are in good agreement. In addition, Figure 2(b) shows that in the first $60 \mu\text{m}$ length span, there is a rapid decline in the power of the TE00 mode and a progressive increase in

the TEM₀₂ mode power. Beyond this position, the interference created between the two modes creates low intensity zones below the metal plugs that effectively decrease not only the loss due to the metal absorption but also the coupling between the modes. Hence, a sort of quasi-zero loss equilibrium condition is reached beyond this position where the two modes propagate in tandem sustaining the beating pattern and where the power decreases gently. The other peaks appearing in the TE₀₀ mode numerically calculated transmission spectrum stem from beating patterns created in a similar manner due to coupling from the TE₀₀ mode to other higher order modes of the nano-ridge.

3. Round-trip laser model

To develop a model for the round-trip gain, we start from the left facet and consider the general case where the TE₀₀ and TEM₀₂ modes are launched with normalized amplitudes of a_1 and a_2 as shown in Figure 3. The modes propagate a length L and reach the right facet with normalized amplitudes a'_1 and a'_2 . Upon reflection, the modes have amplitudes b'_1 and b'_2 , changing to b''_1 and b''_2 when reaching the left facet after a further propagation over a length L . The round-trip is finalized with a reflection, resulting in amplitudes b_1 and b_2 .

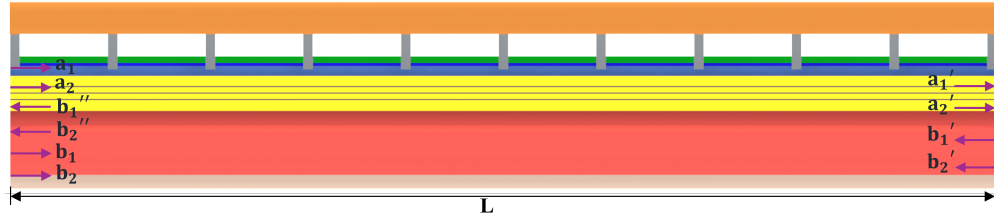


Fig. 3. Schematics showing longitudinal cross-section (along the dashed blue line in Figure 1(a)) of a nano-ridge waveguide with metal plug grating and end facets for round-trip laser model.

Utilizing the results obtained in the previous section, we then find

$$\begin{bmatrix} b_1 \\ b_2 \end{bmatrix} = R \times T \times R \times T \times \begin{bmatrix} a_1 \\ a_2 \end{bmatrix} \quad (9)$$

$$\text{where } T = \begin{bmatrix} (\cos sL - j\frac{\delta}{s} \sin sL)e^{-j(\tilde{\beta} + \frac{1}{\lambda})L} & -j\frac{\kappa_{12}}{s} \sin(sL)e^{-j(\tilde{\beta} + \frac{1}{\lambda})L} \\ -j\frac{\kappa_{21}}{s} \sin(sL)e^{-j(\tilde{\beta} - \frac{1}{\lambda})L} & (\cos sL + j\frac{\delta}{s} \sin sL)e^{-j(\tilde{\beta} - \frac{1}{\lambda})L} \end{bmatrix} \text{ and } R = \begin{bmatrix} r_{11} & r_{12} \\ r_{21} & r_{22} \end{bmatrix}.$$

The reflection coefficients at the facets are defined as:

$$r_{ij} = \left. \frac{b'_i}{a'_j} \right|_{a'_k=0, k \neq j} \quad i = 1, 2, \quad j = 1, 2, \quad k = 1, 2.$$

We evaluated these reflection coefficients by FDTD simulations to be $r_{11} = 0.60$, $r_{12} = r_{21} = 0.24$ and $r_{22} = 0.82$ at the $1.035 \mu\text{m}$ wavelength.

The other parameters are as defined in section 2, except that the propagation constants now also include gain and extra losses. The extra losses are due to scattering, leakage to the substrate

and free-carrier absorption in the doped regions i.e.

$$\beta_i = \frac{2\pi n_i}{\lambda} + j\frac{1}{2}\Gamma_i g_m - j\frac{1}{2}\alpha_{d,i} - j\frac{1}{2}\alpha_{s,i}, \Gamma_i = \frac{\int_{QW} U_i^2 dA}{\int U_i^2 dA}, i = 1, 2.$$

Γ_1 and Γ_2 are the transverse confinement factors for the TE00 and the TEM02 modes in the three $\text{In}_{0.2}\text{Ga}_{0.8}\text{As}$ quantum well (QW) regions respectively hence the designation QW in the overlap integrals. The material gain for the quantum wells is denoted as g_m , $\alpha_{d,1}$ and $\alpha_{d,2}$ correspond to losses associated with free-carrier absorption in the doped regions and $\alpha_{s,1}$ and $\alpha_{s,2}$ are the losses due to scattering and leakage to the substrate for the TE00 and the TEM02 modes respectively.

The scattering and substrate leakage losses were determined from loss measurements of undoped nano-ridge waveguides without the tungsten plugs using the Hakki-Paoli method [30]. A loss of $8 \pm 0.5 \text{ cm}^{-1}$ was found for a 3.5 mm long device. Similar results were obtained for varying waveguide sizes and device lengths. Losses due to coherent scattering into non-guided modes caused by the periodic tungsten contacts are assumed to be small compared to other loss mechanisms. This is because the pitch is several times larger than the working wavelength, leading to low coupling efficiencies from higher-order diffraction. This assumption is further supported by the results in section 2, where we demonstrated good agreement between FDTD simulations and analytical expressions that do not account for such scattering phenomena.

The free-carrier absorption losses in the doped regions for the TE00 and the TEM02 modes were calculated with the FDE mode solver by introducing the imaginary part of the refractive indices of the doped materials. We used the doping profile shown in Figure 1(b), which is based on TEM images for the physical dimensions and an estimation of the carried density through Scanning Spreading Resistance Microscopy (SSRM) and the growth recipe used. Data for the absorption coefficients of phosphorus doped n-Si [31], silicon doped n-GaAs [32], and carbon doped p-GaAs [33,34] were used to set up the refractive indices of the materials in the solver. The losses due to free-carrier absorption thus obtained are 5.2 cm^{-1} and 11.6 cm^{-1} for the TE00 mode and the TEM02 mode respectively.

Now, to further simplify terms, we can write (9) as

$$\begin{bmatrix} b_1 \\ b_2 \end{bmatrix} = \begin{bmatrix} x_{11} & x_{12} \\ x_{21} & x_{22} \end{bmatrix} \begin{bmatrix} a_1 \\ a_2 \end{bmatrix} \quad (10)$$

where the 2×2 matrix on the right side is the product of the four 2×2 matrices on the right side of (9). Lasing will occur for an eigenvalue 1 of this matrix. This insures that the electric field exactly replicates itself after a round-trip. Under this condition,

$$x_{11}x_{22} - x_{12}x_{21} - x_{11} - x_{22} + 1 = 0 \quad (11)$$

Using 11, we calculated the threshold gain to be 792 cm^{-1} for a device with length of $1502.4 \mu\text{m}$. To obtain this value, we employed an iterative process that starts with a certain gain value and solves for the eigenvalue magnitude and then makes small changes in the gain until we obtain an eigenvalue magnitude of 1. Figure 4(a) shows the calculated eigenvalue magnitude and phase vs. wavelength, at threshold. For the wavelengths marked by red points, the round-trip phase equals an integer multiple of 2π . The point at 1035.65 nm satisfies the laser condition. The eigenvector of the round-trip matrix with an eigenvalue of 1 provides the specific combination of the amplitudes a_1 and a_2 necessary for lasing in the cavity. Our analysis reveals that this combination consists of 89% of the TE00 mode power and 11% of the TEM02 mode power at $z = 0$, resulting in lasing at a wavelength of approximately $1.035 \mu\text{m}$.

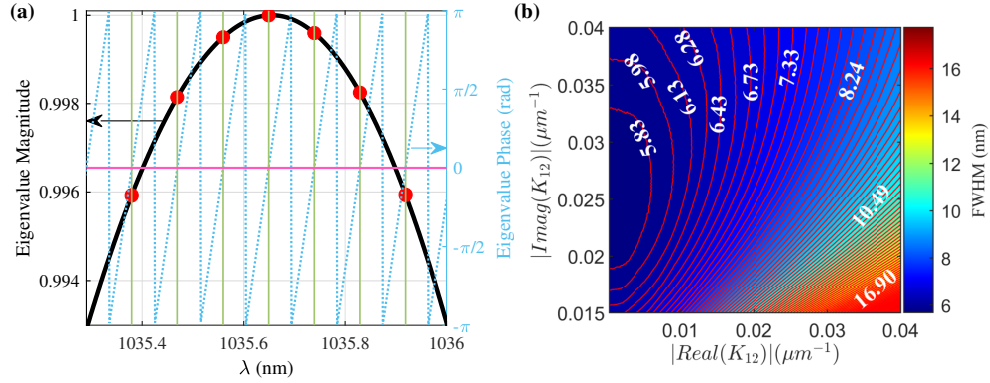


Fig. 4. (a) Eigenvalue magnitude and phase (points in red color have zero phase (at intersections of the green lines and the pink line) and a magnitude close to 1). (b) Contour plot showing the dependence of the FWHM of the eigenvalue magnitude on the real and imaginary parts of $\kappa_{12} = \kappa_{21}$.

In addition, the full width at half maximum (FWHM) of the round-trip gain is a critical parameter in determining the multi-modal nature of the laser as it affects the gain margin. To that end, we investigated the dependence of the FWHM of the eigenvalue magnitude on the real and imaginary parts of the coupling coefficient between the modes, $\kappa_{12} = \kappa_{21}$. By changing the real and imaginary parts of the coupling coefficient around the calculated value at threshold of $(0.01386 - i0.01985) \mu\text{m}^{-1}$, we can see from Figure 4(b) that there is, in general, a decrement in the FWHM as we decrease the real part of the coupling coefficient, the effect being more pronounced when the magnitude of the imaginary part is smaller. Again, we can notice that for a magnitude of the imaginary part less than $0.025 \mu\text{m}^{-1}$, the FWHM decreases with the imaginary value. This decrement is more prominent for larger real values. Beyond an imaginary value of $0.025 \mu\text{m}^{-1}$, the impact is weaker as can be seen from the contour plot.

The model gives us the opportunity to study the effect of different device parameters on the threshold gain and the emission wavelength. For instance, by changing the height of the GaAs box (indicated by letter *a* in Figure 1(b)) from 460 nm to 520 nm, keeping the ratio of the dimensions *g* (the distance from the top of the upper QW to the top of the GaAs box) and *h* (the distance from the top of the trench to the bottom of the lowest QW) constant at 0.72, the wavelength which leads to the lowest loss interference pattern between both modes changes from 950 nm to 1120 nm. This helps us in choosing device dimensions that lead to a substantial overlap with the previously measured gain peak of the nano-ridges which is around 1020 nm [25,35]. In addition, when sweeping the height from 460 nm to 520 nm there is an associated increase in the threshold gain from 745 cm^{-1} to 881 cm^{-1} as depicted in Figure 5(a).

The impact of the GaAs box height on the threshold gain is determined by a cumulative effect of variations of several factors, which include the coupling coefficients (shown in Table 2), the confinement factors in the QW's (shown in Figure 5(b)), the reflection scattering coefficients (shown in Figure 5(c)), the power of the TE₀₀ and the TEM₀₂ modes comprising the eigenvector (shown in Figure 5(d)) and the free-carrier absorption losses in the doped regions (shown in Table 2). The changes in the coupling coefficients are in turn caused by changes in the mode overlaps with the metal contact and the wavelength dependent imaginary part of the refractive index of tungsten. Among these factors, we can notice that an increase in the box height is associated with a decrease in the confinement factor of the TE₀₀ mode (Figure 5(b)) and a decrease in the power of the TEM₀₂ mode of the eigenvector (Figure 5(d)), which has the larger facet reflection compared to the TE₀₀ mode. Moreover, there is a slight decrement in the

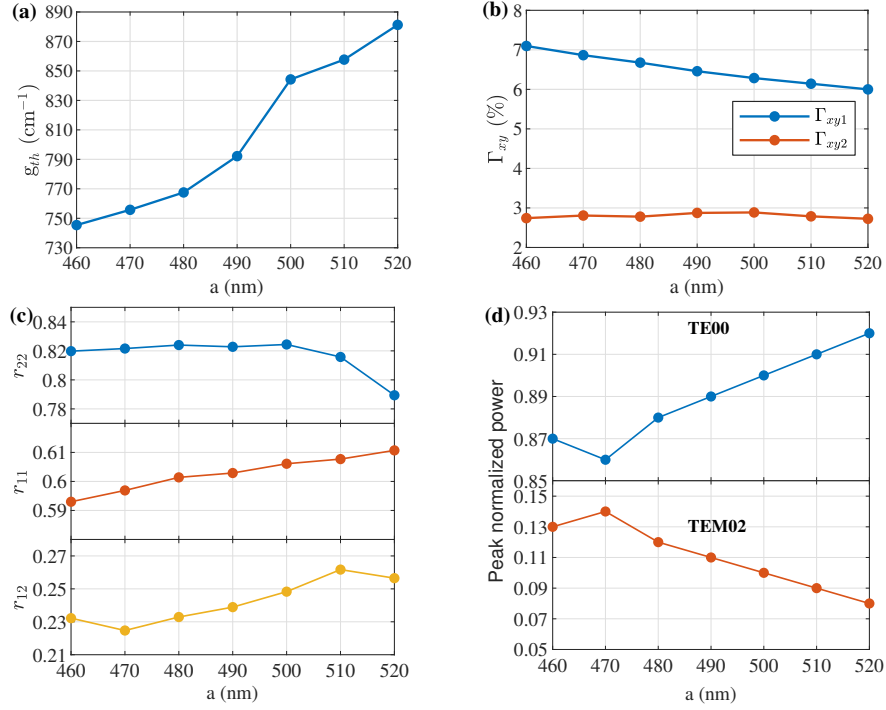


Fig. 5. For different nano-ridge box heights (dimension a in Fig. 1 (b)): (a) Threshold gain. (b) Mode confinement factor in the QW's for the TE00 mode (Γ_1) and the TEM02 mode (Γ_2). (c) Reflection scattering coefficients at lasing wavelengths. (d) Proportion of the power of the TE00 and the TEM02 modes at the left facet.

Table 2. Coupling coefficients and losses in doped regions for varying nano-ridge box heights (a in Fig. 1(b)) at lasing wavelengths

a (nm)	κ_{11} (μm^{-1})	$\kappa_{12} = \kappa_{21}$ (μm^{-1})	κ_{22} (μm^{-1})	$\alpha_{d,1}$ (cm^{-1})	$\alpha_{d,2}$ (cm^{-1})
460	0.0073 - $i0.0106$	0.0139 - $i0.0201$	0.0295 - $i0.0425$	5.00	12.25
470	0.0072 - $i0.0104$	0.0136 - $i0.0197$	0.0286 - $i0.0415$	5.00	12.65
480	0.0071 - $i0.0102$	0.0137 - $i0.0199$	0.0297 - $i0.0429$	5.09	11.76
490	0.0071 - $i0.0102$	0.0139 - $i0.0198$	0.0302 - $i0.0432$	5.17	11.59
500	0.0071 - $i0.0100$	0.0141 - $i0.0198$	0.0309 - $i0.0435$	5.14	11.47
510	0.0071 - $i0.0099$	0.0142 - $i0.0196$	0.0314 - $i0.0435$	5.05	11.83
520	0.0073 - $i0.0098$	0.0145 - $i0.0195$	0.0322 - $i0.0433$	5.17	12.44

magnitude of the imaginary part of the coupling coefficient between the modes ($\kappa_{12} = \kappa_{21}$) that leads to a decrement in the eigenvalue magnitude. All these factors bring about an increase in the threshold gain.

Meanwhile, we also calculated the differential quantum efficiency considering optical power detection by a wide area detector using

$$\eta_d = \frac{2P_{out}}{\Gamma_1 g_{th} \int_0^L (P_{f1} + P_{b1}) dz + \Gamma_2 g_{th} \int_0^L (P_{f2} + P_{b2}) dz} \quad (12)$$

where, P_{out} is the total normalized power of the two modes out of one facet, P_{f1} and P_{f2} represent the normalized power of the forward propagating TE00 and TEM02 modes respectively, and g_{th} is the threshold gain. P_{b1} and P_{b2} depict the normalized power of the modes in the backward direction. η_d is the differential quantum efficiency. An injection efficiency of 100% was assumed in the calculations.

Figures 6(a) and 6(b), respectively, show the differential quantum efficiency and the FWHM of the eigenvalue magnitude spectra as we vary the GaAs box height. The differential quantum efficiency values are relatively low due to the large device length of 1.5 mm. We notice that there is a small increment in the FWHM as we increase the box height. This variation arises from the changes in the coupling coefficient between the modes ($\kappa_{12} = \kappa_{21}$) as discussed earlier in this section and shown by the contour plot in Figure 4(b). The slight increase in the FWHM is attributed to either an increase in the real part, a decrease in the imaginary part, or by a combined effect of both factors in the coupling coefficients ($\kappa_{12} = \kappa_{21}$), as can be noted from Table 2.

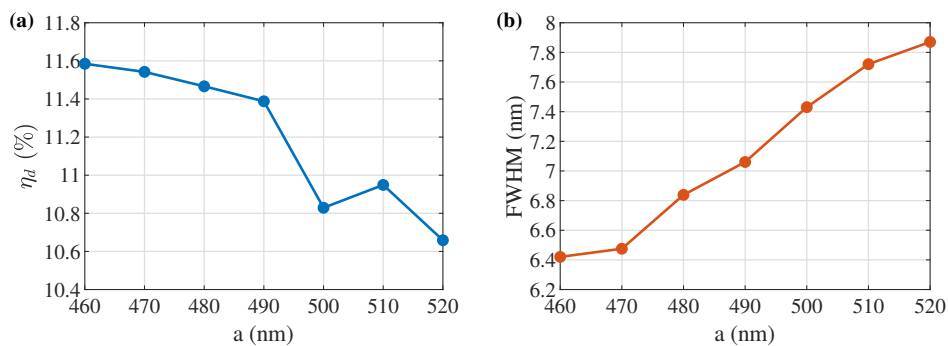


Fig. 6. (a) Differential quantum efficiency. (b) FWHM of the eigenvalue magnitude spectra.

4. Verification of model with experimental results

In this section, we will use the results of the round-trip model discussed in section 3 to study laser emission spectra and threshold gain values for different contact pitches and to compare these results with measurement results from fabricated devices. As briefly explained in the introduction, the growth mechanism, the material stack and device dimensional parameters of these GaAs nano-ridges were exhaustively described in previous works [24,25,27,35]. One particular parameter that is of high significance is the trench width (f in Figure 1(b)). Nano-ridges with larger trench width have larger height (a in Figure 1(b)) and width (b in Figure 1(b)).

By inspecting the transmission electron microscopy (TEM) images of a transverse cross-section of nano-ridge lasers for detailed device dimensions, we calculated mode effective refractive indices, electric field data, reflection scattering coefficients, free-carrier absorption losses due to dopants and mode confinement factors using FDTD and FDE simulations. The laser cavity is realized by two facets, which are formed by dry etching and having an angle of 12° [27].

We first investigated the dependence of the spectral properties of an 80 nm trench nano-ridge on the metal contact pitch. From our model, we found that the loss spectrum for the TE00 mode shows a minimum as a result of mode beating between the TE00 and the TEM01 modes. The lasing wavelengths evaluated by our model for contact pitches of $4.7 \mu\text{m}$, $4.8 \mu\text{m}$ and $4.9 \mu\text{m}$ are shown in Fig. 7(a). We then compared these with the measured lasing wavelengths of electrically-injected nano-ridge lasers having 80 nm trench width and contact pitches of $4.7 \mu\text{m}$, $4.8 \mu\text{m}$ and $4.9 \mu\text{m}$. The measured emission wavelengths for the lasers versus the contact pitches and the corresponding spectra are shown in Figs. 7(b) and 7(c) respectively. All

spectral measurements were conducted at a drive current of 20 mA, with light collected through a horizontal coupling scheme using a lensed single-mode fiber, which was connected to an optical spectrum analyzer.

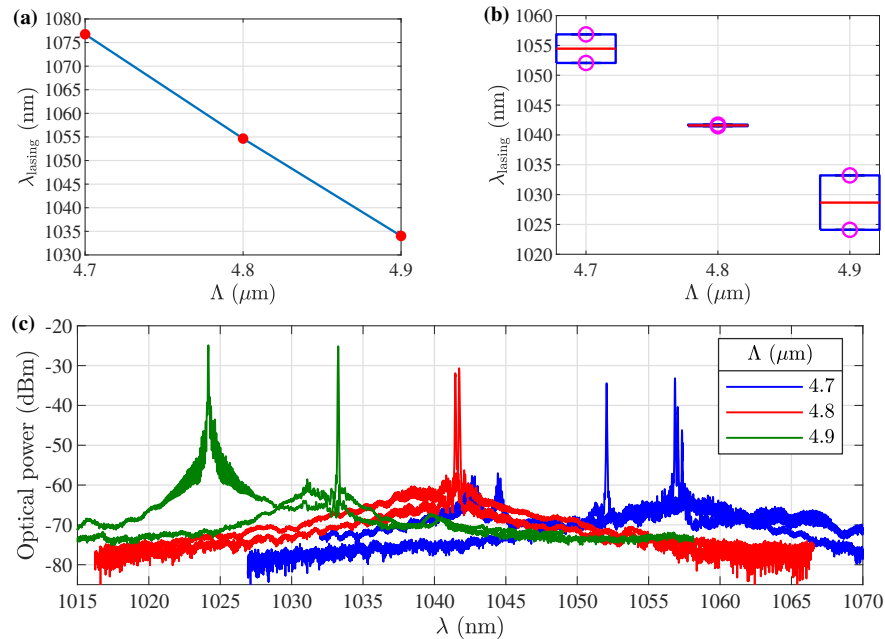


Fig. 7. (a) Model result showing blue shifting of lasing wavelength as we increase the contact pitch from 4.7 μm to 4.9 μm . (b) Measured lasing wavelength versus contact pitch for the spectra in 7(c) showing blue shifting upon increasing contact pitches. (c) Measured spectra for electrically injected nano-ridge laser samples having 80 nm trench width and contact pitches of 4.7 μm , 4.8 μm and 4.9 μm .

One can observe from the results of the model in Fig. 7(a) and the measurement results in Fig. 7(b) that there is around 40 nm blue shifting of the spectra for the model and around 30 nm blue shifting of the spectra for the measured devices as we increase the contact pitch from 4.7 μm to 4.9 μm . In that sense, we can confirm that the model and the experimental results are in agreement. The blue shift originates from the increase in the difference between the effective indices of the TE₀₀ and TEM₀₂ modes as a function of wavelength in the expression for the detuning parameter (δ) in section 2. However, we can also notice from Fig. 7(b) that even for devices having the same trench width and contact pitch there is a variation in the emission wavelengths (around 10 nm for the 4.9 μm contact pitch and around 5 nm for the 4.7 μm contact pitch). This could emanate from slight variations in the device dimensions along the length of the nano-ridge as a result of wafer non-uniformity [27]. We have already seen in the previous section that small changes in the height of the nano-ridges alone can lead to large spectral shifts of the lasing wavelength (around 30 nm change in the peak wavelength for 10 nm change in the height). In addition to this, the differences in the emission wavelengths between the model and the measured spectra could be attributed to the small variations in the refractive index between the actual material stack and the values taken from the material data base of the solvers.

Additionally, we also explored the effect of the threshold gain on the lasing properties of measured devices on two dies from the same wafer having 80 nm trench nano-ridges. To that end, we extracted the dimensions of 3 devices on die 1 having contact pitches of 3.6 μm , 4.8 μm and 5.4 μm and repeated this for 3 more devices on die 2 and used our model to determine their

threshold gain. Figures 8(a) and 8(b) show the calculated threshold gain vs. device length for the 80 nm trench nano-ridges on die 1 and die 2 with contact pitches of 3.6 μm , 4.8 μm and 5.4 μm . The plots also reveal the mode that, in combination with the fundamental TE₀₀ mode, creates the beating pattern responsible for minimizing losses at specific contact pitches.

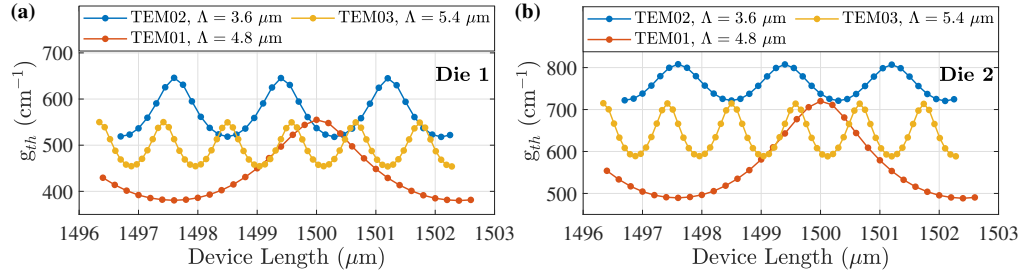


Fig. 8. Calculated threshold gain for 80 nm trench nano-ridge devices on two dies with contact pitches of 3.6 μm , 4.8 μm and 5.4 μm . Included also are the corresponding higher order modes that are coupled with the TE₀₀ mode.

To accommodate possible variation of the device length during the etching operation, we calculated the threshold gain values over a range of 5 μm for 1.5 mm length devices. As we slightly change the device length, we can see from Figures 8(a) and 8(b) that the threshold gain also varies in a periodic fashion with the lowest threshold gain values occurring when we have integer multiples of the beating length fitting in the device length. In this scenario, there is constructive interference between the forward wave beating pattern and the backward wave beating pattern ultimately ensuring the contacts are positioned at the points of lowest intensity. It is important to note that altering the device length also changes the relative position of the right hand side facet with respect to the last metal plug. The eigenvector (combination of the modes involved in the beating) also changes as we change the length of the device and hence plays a role in the overall threshold gain. Furthermore, the loss that originates from the mode overlaps with the metal contact is a crucial factor in these devices. This loss manifests itself in the imaginary part of $\tilde{\beta}$ in Eq. (9) through the self-coupling coefficients (κ_{11} and κ_{22}). We can observe from Table 3 that the magnitude of the imaginary values are higher for κ_{22} compared to κ_{11} owing to the larger mode overlaps with the metal contact for the higher order modes in contrast to the fundamental TE₀₀ mode. The imaginary part of κ_{22} is in turn the smallest for the TEM₀₁ mode and the highest for the TEM₀₂ mode. This contributes to the lower threshold gain values found for the devices with 4.8 μm contact pitch that rely on the TE₀₀/TEM₀₁ beating pattern.

Table 3. Coupling coefficients for devices in Fig. 8 at lasing wavelengths

Die	Λ (μm)	Coupled mode	κ_{11} (μm^{-1})	$\kappa_{12} = \kappa_{21}$ (μm^{-1})	κ_{22} (μm^{-1})
1	3.6	TEM ₀₂	0.0040 – i 0.0051	0.0103 – i 0.0134	0.0280 – i 0.0364
1	4.8	TEM ₀₁	0.0025 – i 0.0036	0.0050 – i 0.0070	0.0098 – i 0.0139
1	5.4	TEM ₀₃	0.0022 – i 0.0032	0.0068 – i 0.0097	0.0236 – i 0.0337
2	3.6	TEM ₀₂	0.0045 – i 0.0056	0.0118 – i 0.0145	0.0320 – i 0.0394
2	4.8	TEM ₀₁	0.0026 – i 0.0037	0.0052 – i 0.0072	0.0103 – i 0.0144
2	5.4	TEM ₀₃	0.0023 – i 0.0032	0.0071 – i 0.0101	0.0252 – i 0.0356

Figure 8 reveals that the threshold gain is indeed smallest over a large length span for the 4.8 μm contact pitch devices, which have been found lasing. On the contrary, the 3.6 μm and 5.4

μm devices are not lasing for these particular devices and this may originate from the relatively larger threshold gain values.

5. Conclusion

We presented a semi-analytical model for electrically injected monolithic nano-ridge lasers. We derived analytical expressions that explain the codirectional coupling between the modes in a nano-ridge waveguide with a tungsten metal contact grating on top and verified the results by using 3D FDTD simulations. The interference pattern created between the fundamental TE₀₀ mode and a higher order mode results in low intensity zones below the metal plugs that effectively decrease not only the loss due to metal absorption but also the coupling between the modes, leading to a low loss equilibrium condition where the power in the two modes decreases gently. We showed how the round-trip model helps in investigating the spectral behavior, the threshold gain and the slope efficiency of lasing devices. Taking detailed device dimensions from the transmission electron microscopy (TEM) images of cross-sections of nano-ridge samples, the dependence of the emission wavelength on the contact pitch and the effect of the threshold gain on the lasing behavior were studied and compared with experimental results. There is, in general, a good agreement between the model and the experimental results albeit with some variation in the lasing wavelengths that could arise due to fabrication variations and uncertainty in the refractive indices data.

We believe that the semi-analytical model can be readily adopted to other device architectures that exploit loss dips originating from a beating between the fundamental mode and higher order modes.

Funding. H2020 Excellent Science (884963).

Acknowledgments. This work was supported by the EU H2020 program under grant agreement No. 884963 (ERC AdG NARIOS). G. Morthier acknowledges Interreg-Lightup and PhotonDelta for financial support.

Disclosures. The authors declare no conflicts of interest.

Data availability. Data underlying the results presented in this paper are not publicly available at this time but may be obtained from the authors upon reasonable request.

References

1. R. Soref and B. Bennett, "Electrooptical effects in silicon," *IEEE J. Quantum Electron.* **23**(1), 123–129 (1987).
2. R. Soref, "The past, present, and future of silicon photonics," *IEEE J. Sel. Top. Quantum Electron.* **12**(6), 1678–1687 (2006).
3. N. Margalit, C. Xiang, S. M. Bowers, *et al.*, "Perspective on the future of silicon photonics and electronics," *Appl. Phys. Lett.* **118**(22), 220501 (2021).
4. S. Y. Siew, B. Li, F. Gao, *et al.*, "Review of silicon photonics technology and platform development," *J. Lightwave Technol.* **39**(13), 4374–4389 (2021).
5. K. Ohashi, K. Nishi, T. Shimizu, *et al.*, "On-chip optical interconnect," *Proc. IEEE* **97**(7), 1186–1198 (2009).
6. C. Minkenberg, R. Krishnaswamy, A. Zilkie, *et al.*, "Co-packaged datacenter optics: Opportunities and challenges," *IET Optoelectron.* **15**(2), 77–91 (2021).
7. Y. Liu, S. Wang, J. Wang, *et al.*, "Silicon photonic transceivers in the field of optical communication," *Nano Communication Networks* **31**, 100379 (2022).
8. S. Lin, X. Zheng, J. Yao, *et al.*, "Efficient, tunable flip-chip-integrated III-V/Si hybrid external-cavity laser array," *Opt. Express* **24**(19), 21454–21462 (2016).
9. S. Bao, Y. Wang, K. Lina, *et al.*, "A review of silicon-based wafer bonding processes, an approach to realize the monolithic integration of Si-CMOS and III-V-on-Si wafers," *J. Semicond.* **42**(2), 023106 (2021).
10. C. Xiang, W. Jin, D. Huang, *et al.*, "High-performance silicon photonics using heterogeneous integration," *IEEE J. Sel. Top. Quantum Electron.* **28**(3), 1–15 (2021).
11. Y. Hu, D. Liang, and R. G. Beausoleil, "An advanced III-V-on-silicon photonic integration platform," *Opto-Electron. Adv.* **4**(9), 200094 (2021).
12. J. Justice, C. Bower, M. Meitl, *et al.*, "Wafer-scale integration of group III-V lasers on silicon using transfer printing of epitaxial layers," *Nat. Photonics* **6**(9), 610–614 (2012).
13. J. Zhang, G. Muliuk, J. Juvert, *et al.*, "III-V-on-Si photonic integrated circuits realized using micro-transfer-printing," *APL Photonics* **4**(11), 110803 (2019).

14. G. Roelkens, J. Zhang, L. Bogaert, *et al.*, "Micro-transfer printing for heterogeneous Si photonic integrated circuits," *IEEE J. Sel. Top. Quantum Electron.* **29**(3: Photon. Elec. Co-Inte. and Ad), 1–14 (2022).
15. J. Van der Ziel, R. Dupuis, R. Logan, *et al.*, "Degradation of GaAs lasers grown by metalorganic chemical vapor deposition on Si substrates," *Appl. Phys. Lett.* **51**(2), 89–91 (1987).
16. D. Jung, Z. Zhang, J. Norman, *et al.*, "Highly reliable low-threshold InAs quantum dot lasers on on-axis (001) Si with 87% injection efficiency," *ACS Photonics* **5**(3), 1094–1100 (2017).
17. J. Selvidge, J. Norman, E. T. Hughes, *et al.*, "Defect filtering for thermal expansion induced dislocations in III-V lasers on silicon," *Appl. Phys. Lett.* **117**(12), 122101 (2020).
18. C. Shang, J. Selvidge, E. Hughes, *et al.*, "A pathway to thin GaAs virtual substrate on on-axis Si (001) with ultralow threading dislocation density," *Phys. Status Solidi A* **218**(3), 2000402 (2021).
19. W.-Q. Wei, A. He, B. Yang, *et al.*, "Monolithic integration of embedded III-V lasers on SOI," *Light: Sci. Appl.* **12**(1), 84 (2023).
20. Z. Wang, B. Tian, M. Pantouvaki, *et al.*, "Room-temperature InP distributed feedback laser array directly grown on silicon," *Nat. Photonics* **9**(12), 837–842 (2015).
21. L. Megalini, B. Bonef, B. C. Cabinian, *et al.*, "1550-nm InGaAsP multi-quantum-well structures selectively grown on v-groove-patterned SOI substrates," *Appl. Phys. Lett.* **111**(3), 032105 (2017).
22. Y. Han, W. K. Ng, Y. Xue, *et al.*, "Telecom InP/InGaAs nanolaser array directly grown on (001) silicon-on-insulator," *Opt. Lett.* **44**(4), 767–770 (2019).
23. Y. Han, Y. Xue, Z. Yan, *et al.*, "Selectively grown III-V lasers for integrated Si-photonics," *J. Lightwave Technol.* **39**(4), 940–948 (2021).
24. B. Kunert, W. Guo, Y. Mols, *et al.*, "Integration of III/V hetero-structures by selective area growth on Si for nano-and optoelectronics," *ECS Trans.* **75**(8), 409–419 (2016).
25. Y. Shi, Z. Wang, J. Van Campenhout, *et al.*, "Optical pumped InGaAs/GaAs nano-ridge laser epitaxially grown on a standard 300-mm Si wafer," *Optica* **4**(12), 1468–1473 (2017).
26. D. Colucci, M. Baryshnikova, Y. Shi, *et al.*, "Unique design approach to realize an O-band laser monolithically integrated on 300 mm Si substrate by nano-ridge engineering," *Opt. Express* **30**(8), 13510–13521 (2022).
27. Y. De Koninck, C. Caer, D. Yulistira, *et al.*, "GaAs nano-ridge laser diodes fully fabricated in a 300-mm cmos pilot line," *Nature* **637**(8044), 63–69 (2025).
28. "Lumerical photonics simulation and design software official website," <http://https://www.ansys.com/products/photonics>. Accessed: 2024-02-12.
29. L. A. Coldren, S. W. Corzine, and M. L. Mashanovitch, *Diode lasers and photonic integrated circuits*, (John Wiley & Sons, 2012), chap. 6.
30. S. Taebi, M. Khorasaninejad, and S. S. Saini, "Modified Fabry-Perot interferometric method for waveguide loss measurement," *Appl. Opt.* **47**(35), 6625–6630 (2008).
31. S. C. Baker-Finch, K. R. McIntosh, D. Yan, *et al.*, "Near-infrared free carrier absorption in heavily doped silicon," *J. Appl. Phys.* **116**(6), 063106 (2014).
32. J.-P. Weber, "Optimization of the carrier-induced effective index change in InGaAsP waveguides-application to tunable bragg filters," *IEEE J. Quantum Electron.* **30**(8), 1801–1816 (1994).
33. K. Kiyota, T. Kageyama, H. Shimizu, *et al.*, "Measurement of absorption coefficient of carbon-doped GaAs," *Jpn. J. Appl. Phys.* **48**(11), 111103 (2009).
34. D. I. Babic, J. Piprek, K. Streubel, *et al.*, "Design and analysis of double-fused 1.55 μm vertical-cavity lasers," *IEEE J. Quantum Electron.* **33**(8), 1369–1383 (1997).
35. B. Kunert, W. Guo, Y. Mols, *et al.*, "III/V nano ridge structures for optical applications on patterned 300 mm silicon substrate," *Appl. Phys. Lett.* **109**(9), 091101 (2016).